Supporting Information

Highstein et al. 10.1073/pnas.1319561111

SI Text

Zero Current Potential and Ionic Concentrations in the Cleft. Present data show that the nonquantal excitatory postsynaptic current (nqEPSC) was carried by K^+ and Na^+. Accounting for both ions, the Goldman–Hodgkin–Katz zero current potential E_{nq} of the nqEPSC is given by

$$E_{nq} = \frac{RT}{F(1+P_{Na/K})}\left(\ln\left(\frac{[K^+]}{120}\right) + P_{Na/K}\ln\left(\frac{[Na^+]}{5}\right)\right), \quad \textbf{[S1]}$$

where R is the ideal gas constant, T is absolute temperature, and F is Farraday's constant. $[K^+]$ and $[Na^+]$(mM) are extracellular concentrations in the cleft, 120 and 5 mM are intracellular concentrations set by the recording pipette, and $P_{Na/K}$ is the permeability to Na^+ re: K^+. It has been shown previously that K^+ entering the cleft from hair cells can increase cleft $[K^+]$ well beyond that of the extracellular space (1), and hence, concentrations in the extracellular media cannot be used to estimate concentrations in the cleft. To estimate $[K^+]$ and $[Na^+]$ concentrations in the cleft, we used zero current potentials in normal extracellular media and when extracellular $[Na^+]$ was replaced with *N-methyl-D-glucamine* (*NMDG*). Both $[K^+]$ and $[Na^+]$ in the cleft changed in the presence of *NMDG*. The zero current potential of the nqEPSC shifted from E_{nq} in normal media to E_{nq}^{NMDG} (mV) in *NMDG*, whereas there was little change in the magnitude of the nqEPSC. These results suggest that the total cationic concentration might be regulated in the cleft and that any gross decreases in $[Na^+]$ might be offset by increases in $[K^+]$. Under this assumption,

$$E_{nq} = \frac{RT}{F(1+P_{Na/K})}\left(\ln\left(\frac{[K^+]}{120}\right) + P_{Na/K}\ln\left(\frac{[T^+]-[K^+]}{5}\right)\right), \quad \textbf{[S2]}$$

where $[T^+]$ is the total $[K^+]$ plus $[Na^+]$. To estimate concentrations, we assumed that $[T^+] = 125$ mM and minimized the cost function $\varepsilon = (E_{nq}^{NMDG} - 15)^2 + (E_{nq} - 44)^2$ numerically (using conservative estimates of $E_{nq} = +44$ and $E_{nq}^{NMDG} = +15$ mV). This approach provided estimates of the relative permeability $P_{Na/K} = 5.2$ and ion concentrations (concentrations in the presence of NMDG: $[K^+]_{CLEFT}^{NMDG} = 115$ mM and $[Na^+]_{CLEFT}^{NMDG} = 10$ mM; concentrations in normal media: $[K^+]_{CLEFT} = 84$ mM and $[Na^+]_{CLEFT} = 41$ mM).

It is important to note that the voltage reported by the amplifier has an implicit error caused by the access series resistance. The error is small at the whole-cell zero-current potential (distinct from E_{nq}) but becomes large as the cell is depolarized by injection of current through the electrode. We used Eqs. **S5** and **S6** below to correct for it before plotting I–V curves and the nqEPSC reversal. The correction was relatively modest, because the whole-cell resistance was quite a bit larger than the electrode access series resistance.

Simple Model for Adapting $[H^+]$ Gated Channel. $[H^+]$ kinetics in the cleft were modeled using a nonlinear single compartment approach accounting for buffering and clearance as described in the text. The single compartment model mimics major features of $[H^+]$ buildup in the cleft observed in the present experiments. Conductance G of the postsynaptic receptor was modeled as increasing with increased unbound free $[H^+]$ in the cleft (either directly or through a second messenger) according to

$$\frac{dG}{dt} + \frac{1}{\tau}G = g\left\{(1-\varphi)\,h\frac{d[H^+]}{dt} + \frac{\varphi}{\tau}[H^+]\right\}, \quad \textbf{[S3]}$$

where τ is the channel adaptation time constant, $0 \le \varphi \le 1$ is the extent of adaptation, g is the gain, and h is the unit Heavyside function ($h = 1$ if $d[H^+]/dt \ge 0$; $h = 0$ otherwise). The nqEPSC was modeled as a chord conductance multiplied by the electrochemical driving potential

$$I = G(V_m - E_{nq}), \quad \textbf{[S4]}$$

where V_m is the membrane potential across the inner leaflet of the calyx facing the cleft, and E_{nq} is the zero current potential of the nqEPSC given in Eq. **S2**. For rapid changes in pH, this model predicts a rapidly increasing current followed by adaptation, and for slow changes in pH, it predicts a slowly modulated current that tracks pH. In the present simulations, we used $\tau = 60$ ms, $\varphi = 0.3$, $E_{nq} = 44$ mV, and $g_1 = 2\times10^{-4}$ S mV^{-1}. Model equations are nonlinear, and therefore, results of simulations were fit with exponential curves to compare time constants with present experimental results.

Several shortcomings of this model are noted. (*i*) $[H^+]$ kinetics were modeled using a single compartment model and therefore, cannot describe large-scale spatial variations in $[H^+]$ that were shown to occur in the calyx (Fig. 4) or hypothetical microscale variations that could occur near clusters of channels. (*ii*) The model assumes a constant H^+ clearance rate k, which in reality, is likely to be voltage- and concentration-dependent. (*iii*) Eq. **S3** describing the receptor is strictly empirical and does not account for any nonlinearity of the postsynaptic current. The single degree-of-freedom simplification (one time constant in Eq. **S2**) clearly prevents the model from capturing the change in time constant occurring near the reversal potential (Fig. 3*A*).

Series Resistance Correction. Electrode and whole-cell capacitance compensation was applied during the recording session. Series resistance was compensated after the experiment using custom software (IgorPro; WaveMetrics). Assuming ideal capacitance compensation and no series resistance compensation, the corrected membrane conduction current I_M was approximated using

$$I_M \approx I_{EC}(1 + R_E/R_M) + C_M R_E \frac{dI_{EC}}{dt}, \quad \textbf{[S5]}$$

where I_{EC} is the amplifier current recorded with capacitance compensation, R_E is the electrode access resistance, R_M is the whole-cell membrane resistance, and C_M is the total capacitance (including membrane and electrode). The corresponding corrected membrane potential was approximated using

$$V_M \approx V_{EC} - R_E I_{EC}, \quad \textbf{[S6]}$$

where V_{EC} is the capacitance-compensated voltage output by the amplifier. To derive these equations, we assumed that voltage-dependent dynamic responses caused by the series resistance-associated loss of voltage clamp were small. These equations were applied in the time domain before data analysis. Because of their slow kinetics, the capacitive component of the correction in Eq. **S5** has no effect on the nqEPSCs, but the series resistance correction does have an effect and acts on both the current and the voltage (Eqs. **S5** and **S6**).

pH Imaging. An animation of stimulus-evoked cleft acidification (Fig. 4) is provided in Movie S1. The animation shows stimulus-evoked acidification at ~70 points in the synaptic cleft based on

$\Delta F/F$ in 1-μm^2 regions of interest. The background image is time-averaged fluorescence. This particular calyx envelops four type I hair cells. A fluid jet was used to deflect the hair bundle of cell 1. The size of each symbol denotes the change in pH, which peaked at −0.2. The lower curve shows ΔpH of the leftmost point (region of interest) adjacent to cell 1. The diagonal yellow bar on cell 1 depicts the hair bundle displacement, which was above the focal plane and not visible during fluorescence acquisition. For fluid jet stimuli, the hair bundle reached its peak displacement with a time constant of ∼29 ms. In a strong 10 mM Hepes buffer, synaptic cleft acid buildup followed a much slower time course and was not limited by the fluid jet. Also, data indicate that endogenous pH buffers in the cleft are likely to be weak (Fig. 5). Based on model simulations, the buffering suggests that cleft acidification under endogenous physiological conditions could be more than threefold faster than observed in the present experiments. Under such conditions, cleft acidification would more closely follow the kinetics of the hair bundle deflection.

Fig. S1 shows an example of stimulus-evoked extracellular acidification of the synaptic cleft (Fig. S1*A*). When filling the patch pipette with the pH indicator carboxylic acid, acetate, succinimidyl ester (SNARF, Life Technologies), nqEPSCs were still present (Fig. S1*B*), but there was no detectable change in fluorescence. These data suggest that protons are not the charge carriers and that the postsynaptic calyx pH_i is nearly constant under voltage-clamp conditions. Present experiments did not patch hair cells or record hair cell pH_i, but based on stimulus-evoked proton extrusion from hair cells reported here and previous results in other cells, one would expect stimulus-evoked modulation of hair cell pH_i (2). Given that the calyx envelops the entire hair cell and the volume of the cleft is small relative to the hair cell intracellular volume, stimulus-evoked calyx cleft acidification might be considerably larger in magnitude than hair cell intracellular acidification.

Acid-Sensing Ion Channel Expression in the Calyx. Although the present results suggest that modulation of the nqEPSC is causal to changes in cleft pH, it is not known if protons directly gate the channel or if a more complex signaling pathway is at play. The channel permeability is consistent with common acid-sensing ion channels (ASICs), but the relatively slow and nonadapting kinetics suggest that the molecular mechanism is unlikely to reflect direct proton gating of a postsynaptic ASIC. Nevertheless, we investigated ASIC expression in our preparation to see if we could rule out this possibility.

Turtles were anesthetized and then perfused through the heart with heparinized (2 U/mL) PBS (0.01 M, pH 7.3) followed by 4% paraformaldehyde in PBS. In other immunostaining experiments, end organs from decapitated turtles were dissected and then immersion-fixed in 4% paraformaldehyde in PBS. After fixation, dissected end organs were rinsed, immersed in blocking buffer (5% normal goat serum in PBS with 0.05% Triton X-100 and 0.02% NaN_3), and then incubated in primary antibody (3 μg/mL; mouse monoclonal anti-ASIC1; Millipore) and rabbit polyclonal anti-ASIC3 (3 μg/mL; BioSciences) diluted in PBS with 5% normal goat serum, 0.01% Triton X-100, and 0.02% NaN_3 (incubation buffer). The samples were subsequently rinsed and incubated in fluorescent-tagged secondary reagents (goat anti-rabbit or anti-mouse IgG; Alexa dyes; Invitrogen) diluted in incubation buffer. Controls included end organs placed in incubation buffer without primary antibody or in an inappropriate secondary reagent (e.g., mouse monoclonal anti-ASIC1 followed by goat anti-rabbit IgG). No specific labeling was observed in these controls. All specimens were imaged with an Olympus FluoView FV1000MPE multiphoton microscope with a Coherent Chameleon Vision II laser tuned to 780 nm and a 25×, 1.05-N.A. immersion objective.

Specific staining for ASIC1 and ASIC3 was observed in association with calyceal endings in both the lagena and the crista ampullares of the anterior and posterior semicircular canals. This labeling included both diffuse immunofluorescence throughout the calyx and small bright puncta located within the calyceal ending. It is not currently known if these channels play a role in the protonergic synaptic transmission reported here, but it seems that we cannot rule out this possibility. The bright puncta are likely to reflect clusters of ASIC channels within discrete regions of the calyx, but it is not known if they colocalize with sites of presynaptic proton extrusion (Fig. 4).

Morphology. We visualized the morphology of individual afferents and calyx terminals by filling the patch pipette with Lucifer yellow. Wide-field epifluorescence was used during the electrophysiological recording session, and in some cases, the tissue was fixed and visualized using confocal microscopy. Morphologies of calyces in the turtle lagena were similar to those reported previously in the turtle crista (3). Examples are provided in Fig. S3. Calyx-only afferents contact a single or multiple type I hair cells (three shown) (Fig. S3*A*). Dimorphic afferents with calyces envelop type I hair cells, and bouton terminals contact type II hair cells (three shown) (Fig. S3 *B* and *C*). In some cases, the dye entered the hair cell, indicating a breach of the inner membrane—these cases were excluded from the present study (Fig. S3*C*).

1. Lim R, Kindig AE, Donne SW, Callister RJ, Brichta AM (2011) Potassium accumulation between type I hair cells and calyx terminals in mouse crista. *Exp Brain Res* 210(3-4): 607–621.
2. Caldwell L, Harries P, Sydlik S, Schwiening CJ (2013) Presynaptic pH and vesicle fusion in Drosophila larvae neurones. *Synapse* 67(11):729–740.
3. Brichta AM, Goldberg JM (2000) Morphological identification of physiologically characterized afferents innervating the turtle posterior crista. *J Neurophysiol* 83(3): 1202–1223.

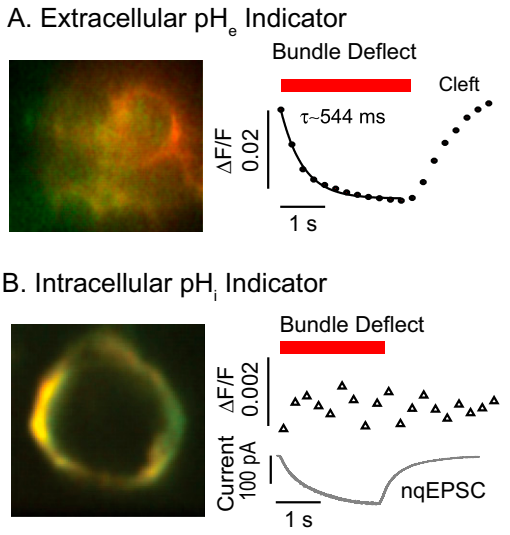

Fig. S1. The pH indicator ratiometric membrane impermeant carboxy SNARF was introduced into (*A*) the extracellular media through the bath or (*B*) the calyx through the voltage-clamp recording pipette. In all cases, the SNARF solution was pH-balanced to match SNARF-free solutions. (*A*, *Left*) Image showing time-averaged extracellular fluorescence around a complex calyx enveloping multiple type I hair cells and (*A*, *Right*) kinetics of spatially averaged extracellular fluorescence modulation (Δ*F*/*F*) in response to a fluid jet-driven hair bundle displacement. (*B*, *Left*) Image showing time-averaged intracellular fluorescence within a simple calyx enveloping a single type I hair cell and (*B*, *Upper Right*) kinetics of spatially averaged intracellular fluorescence modulation (Δ*F*/*F*) in response to fluid jet-driven hair bundle displacement. Intracellular (Δ*F*/*F*) in the postsynaptic calyx was not detectable by the present methods and at least an order of magnitude smaller than Δ*F*/*F* in the extracellular cleft. (*B*, *Lower Right*) nqEPSCs were normal in the presence of the SNARF indicator, showing that the nqEPSC did not acidify the postsynaptic calyx.

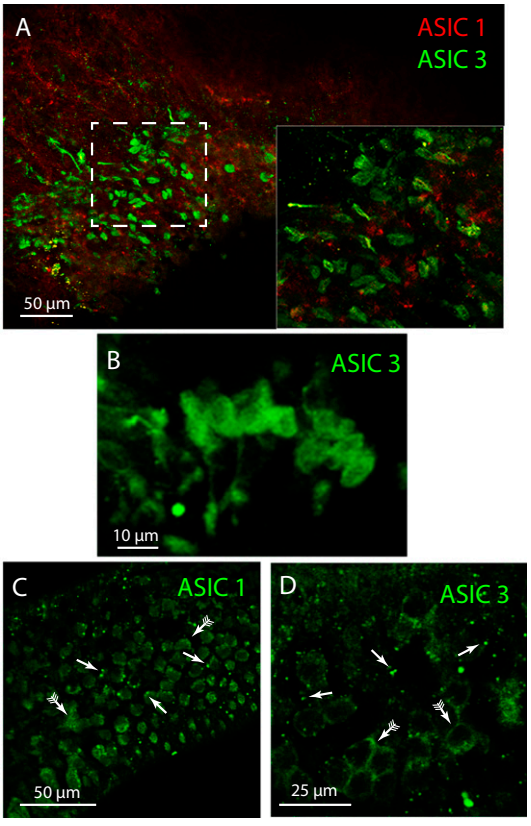

Fig. S2. Immunofluorescence visualization of ASIC1 and ASIC3 in turtle end organs. (*A*) Both punctate and diffuse labeling are associated with calyces in the lagena. The boxed region is shown at a higher magnification in *Inset*. (*B*) The diffuse staining is present in the calyceal cytoplasm. (*C* and *D*) ASIC staining in the turtle canal cristae. Punctate (arrows) and diffuse (feathered arrows) immunolabeling for both channels are associated with calyceal endings.

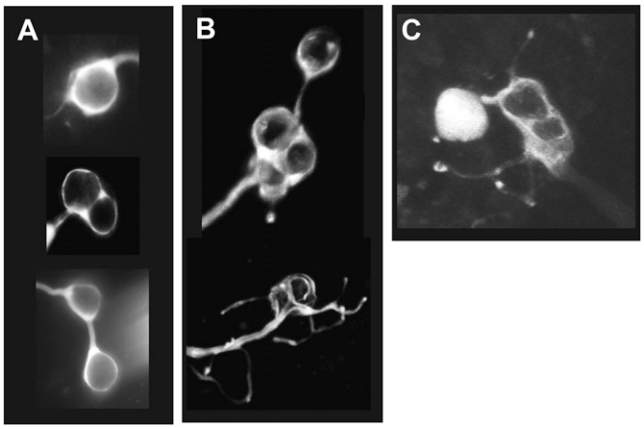

Fig. S3. Calyx morphology. The voltage-clamp patch pipette was filled with Lucifer yellow to visualize the calyx and associated projections. In all cases, cells were patched on the outer leaflet of the calyx terminal adjacent to one of the type I hair cells enclosed by the calyx. The mechanical stimulus was positioned to deflect the type I hair bundle associated with the enclosed hair cell. (*A*) Calyx only and (*B* and *C*) dimorphic units are shown.

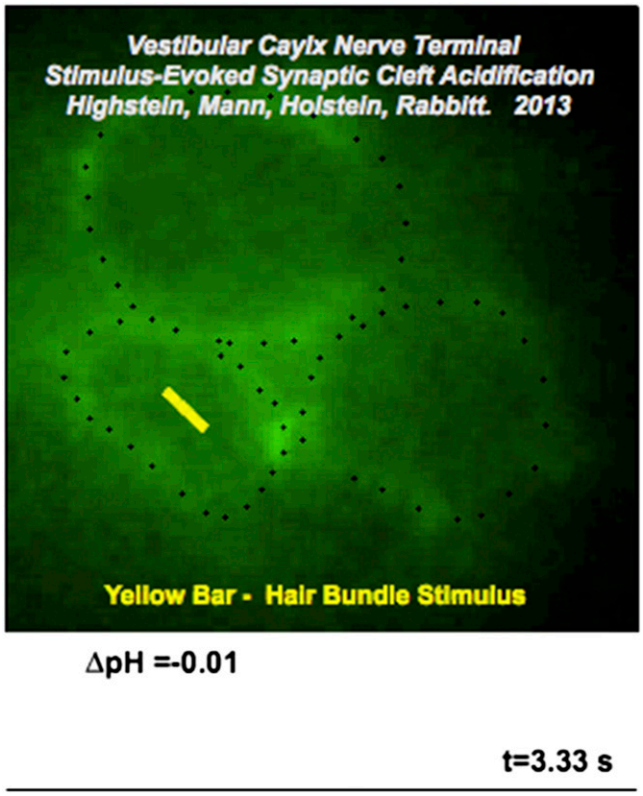

Movie S1. Stimulus-evoked acidification of the vestibular hair cell–calyx synaptic cleft. Background image shows time-averaged fluorescence of the pH indicator impermanent indicator pyrannine H348 added to the media and accumulated in the extracellular space around hair cells viewed perpendicular to the long axis of the cells. A single calyx envelops four hair cells. Synaptic clefts surrounding three hair cells are indicated by circular markers. The hair bundle of one hair cell was deflected with a 0.3-Hz fluid jet as indicated by the yellow bar. The size of each marker indicates the magnitude of the pH change directly under the marker. The largest pH change was around the stimulated hair cell and reached approximately −0.2 pH units. Changes around adjacent hair cells within the same calyx were smaller and time-delayed.

Movie S1